Retrieval of the Characteristic Size of Raindrops for Wind Sensing Based on Dual-Polarization Radar

Yunli Peng , Jianbing Li , *Senior Member, IEEE*, Jiapeng Yin , Pak Wai Chan, Wai Kong, and Xuesong Wang

Abstract—**Wind velocity is of great importance for weather monitoring, aviation hazard alerting, wind energy exploring, etc. Doppler radar is widely used to measure wind under rainy condition by sensing the raindrops entrained by the background wind. However, the Doppler velocity, which is a reflection of the raindrops' velocity in radial direction, is not coincident with the background wind because of the strong inertia of raindrops. Efforts should be made to distinguish the difference between the raindrops' velocity and the background wind velocity. In this article, we try to establish a relationship between the background wind velocity and the raindrops' velocity by introducing a definition of the raindrops' characteristic size, which is related to the velocity characterized by the strongest Doppler spectral component. It is found that the fusion of differential reflectivity and the depolarization ratio can serve as a good proxy for the estimation of the characteristic size. Simulation results for $S/C/X$-band radars and radar measurements verify the good performance of the proposed retrieval model for the characteristic size, which lays a solid foundation for the retrieval of the background wind velocity.**

Index Terms—**Characteristic size of raindrops, depolarization ratio, differential reflectivity, drop size distribution, equivalent radar cross section (RCS), support vector regression (SVR).**

I. INTRODUCTION

THE information of wind is an important factor for weather monitoring, aviation hazard alerting, wind energy exploring, climate studies, etc., and the wind measurement technology has attracted much attention in the past few decades. The instruments for wind detection over large spatial and temporal scales mainly include lidar and radar. Lidar is generally a good option for wind detection in dry air [1]–[3], but its application in wet weather condition is greatly limited due to the heavy propagation attenuation of laser in precipitations. Comparatively, radar performs well in wet weather condition because microwave radiation can propagate through the precipitation with much less attenuation. For ocean surface wind, remote sensing techniques

Yunli Peng, Jianbing Li, Jiapeng Yin, and Xuesong Wang are with the State Key Laboratory of Complex Electromagnetic Environment Effects on Electronics and Information System, College of Electronic Science and Engineering, National University of Defense Technology, Changsha 410073, China (e-mail: yunlipe@163.com; jianbingli@nudt.edu.cn; jiapeng.yin@hotmail.com; wxs1019@vip.sina.com).

Pak Wai Chan and Wai Kong are with the Hong Kong Observatory, Hong Kong (e-mail: pwchan@hko.gov.hk; wkong@hko.gov.hk).

were well investigated [4]–[9], where the main detection mechanism is to retrieve wind information based on the sensitivity of the ocean surface's scattering cross section to the changes of wind velocity. However, for inland wind sensing under rainy condition, the main mechanism is to retrieve the background wind velocity from the Doppler velocity of raindrops entrained by the wind [10]–[12]. However, the Doppler velocity, which is a reflection of the raindrops' velocity, is not coincident with the background wind velocity because of the strong inertia of raindrops [13]. This results in a gap between the background wind velocity and the raindrop's Doppler velocity, and efforts should be made to fix this gap.

It is known that for a certain radar range bin, the Doppler spectrum, which is composed of a lot of spectral components, reveals the ensembling effect of the dynamics of all the raindrops in this range bin. And the most typical method to obtain the Doppler velocity is to extract the velocity at the spectral component with the highest spectral energy. In this manner, if the size of the raindrops corresponding to the strongest Doppler spectral component can be determined, the motion equation of this group of raindrops can be established. This equation presents the relationship between the raindrops' velocity (reflected by the Doppler velocity) and the background wind velocity, making it possible to retrieve the background wind velocity with mathematical techniques. Therefore, a key issue for the above process is to get the raindrop's size for the strongest Doppler spectral component, which is also the main content of this article.

In fact, raindrop size distribution (DSD) and its retrieval technology have been studied in meteorology community for a long time. Since Seliga and Bringi [14] indicated that the polarimetric variables can be used to retrieve the parameters of an exponential DSD model in 1976, plenty of studies have been conducted to explore the relationship between polarimetric variables and raindrop's size. Among them, the gamma distribution [15] and normalized gamma distribution [16] were widely used due to their good adaptability to different rain cases, such as the constrained gamma method [17] and the beta method [18], [19]. And those methods have also been applied to data of different radar bands with the development of dual-polarization radar and the correction technology of attenuation effect.

Even though there have been a lot of efforts to get the DSD of raindrops, the retrieval of a special size that corresponding to the strongest Doppler spectral component has been rarely studied. This size can serve as a bridge to connect the raindrops' velocity (reflected by the Doppler velocity) and background

wind velocity, so it is called the characteristic size in the present study. The main objectives of this study are:

1) to propose a new approach to retrieve the characteristic size directly;

2) to test the performance of retrieval models of the characteristic size with field observation data;

3) to verify the feasibility of retrieval of the background wind velocity with the information of the characteristic size.

The rest of this article is organized as follows. The definition of characteristic size and its impact factors are introduced in Section II. Section III presents the relationship between the characteristic size and polarimetric variables, and a new method to retrieve the characteristic size based on polarimetric variables is proposed. To better verify the performance, the proposed method is implemented to the data around the Hong Kong International Airport (HKIA) from an S-band dual-polarization Doppler weather radar in Hong Kong in Section IV. Section V concludes this article.

II. DEFINITION AND FACTORS OF THE CHARACTERISTIC SIZE OF RAINDROPS

A. Physical Features of Raindrops

In nature, a raindrop in falling is generally nonspherical due to the compression of air resistance, and the deformation for a big raindrop is typically severer than a smaller one. In the community of meteorology, oblate shape is assumed to be a good representative of the shape of a raindrop, and the equivolumetric spherical drop diameter [20] (hereafter, diameter) and axis ratio [21] (i.e., ratio of particle minor-to-major dimension) are always used to characterize the shape. According to the theory of particle's motion, a raindrop of certain diameter falls with certain terminal falling velocity in still air, which is the consequence of equilibrium between the gravity and drag force on this raindrop. According to Atlas *et al.* [22], raindrop's terminal falling velocity can be given with its diameter as

$$V_{\mathrm{T}}(D) = [\alpha_1 - \alpha_2 \exp(-\alpha_3 D)](\rho_0/\rho)^{0.4} \quad (1)$$

where D is the diameter of raindrops, $\alpha_1 = 9.65$, $\alpha_2 = 10.3$, $\alpha_3 = 0.6$, and ρ_0/ρ is ratio of the air densities in the sea surface and at the altitude of measurement. For radar detection in still air, the Doppler velocity is the projection of the terminal falling velocity on the radar beam.

It is well known that a rain case contains a lot of raindrops of different sizes, and there have been a variety of existing DSD models to characterize the size distribution, including the exponential distribution [23], gamma distribution [15], and normalized gamma distribution [16]. The exponential distribution model is given by

$$N(D) = N_0 \exp(-\Lambda D) \quad (2)$$

where N_0 is the scaling parameter and Λ is the slope parameter. The gamma distribution model is given by

$$N(D) = N_{\mathrm{m}}(D)^{\mu_{\mathrm{m}}} \exp(-\Lambda_{\mathrm{m}} D) \quad (3)$$

where N_{m} and Λ_{m} are similar to N_0 and Λ in the exponential distribution model, and μ_{m} is unitless and always fixed on

2 or 3 in most cases. The normalized gamma distribution model is given by

$$N(D)$$
$$= N_{\mathrm{w}} \frac{6(3.67 + \mu)^{\mu+4}}{3.67^4 \Gamma(\mu + 4)} \left(\frac{D}{D_0}\right)^{\mu} \exp\left(\frac{-(3.67 + \mu)D}{D_0}\right) \quad (4)$$

where N_{w} is the normalized intercept parameter, D_0 is the median volume diameter, and μ is the unitless shape parameter. Among them, the exponential distribution model was proven unsuitable for heavy rain cases [24], and the parameters of the gamma distribution model are coupled to each other [25]; they are not applicable to analyze the dominant factors of the characteristic size for all different rainfall types. Comparatively, the normalized gamma distribution model is determined by independent parameters and has good adaptability to different rainfall types in nature [26]. Based on these facts, the normalized gamma distribution is adopted in this study to analyze the issues about the raindrops' characteristic size.

B. Characteristic Size of Raindrops

In a certain radar range bin, plenty of raindrops with different velocities lead to a Doppler spectrum [27], consisting of different characteristic spectral components

$$S(v) = \sigma_{\mathrm{pol}}(D)N(D) \mid dD/dv \mid \quad (5)$$

where $\sigma_{\mathrm{pol}}(D)$ is the backscattering radar cross section (RCS) of a raindrop in terms of different polarizations, $N(D)$ is the DSD in this radar range bin, and $|dD/dv|$ is the Jacobean of diameter to radial velocity transformation. Here, an assumption is made that a group of raindrops with a certain diameter in a radar range bin have the same velocity. In (5), the part that determines the density of the spectrum is defined as equivalent RCS σ_{e}, as shown in the following equation:

$$\sigma_{\mathrm{e}}(D) = \sigma_{\mathrm{pol}}(D)N(D). \quad (6)$$

If the Doppler velocity is obtained from "hh" polarization channel (horizontal polarization for both transmission and reception), then $\sigma_{\mathrm{pol}} = \sigma_{\mathrm{hh}}$. Similarly, $\sigma_{\mathrm{pol}} = \sigma_{\mathrm{vv}}$ if the Doppler velocity is obtained from "vv" polarization channel.

According to the definition of (5), each spectral component should correspond to a group of raindrops of a certain diameter in general. According to fluid dynamics, if the velocity and diameter for a group of raindrops are known, the motion equation for these raindrops can be established to connect the background wind velocity and the raindrops' velocity. But for a given spectral component, which diameter of raindrops' motion does this spectral component reveal? This relationship is not easy to determine.

Of course, the Doppler velocity, which is generally obtained from the strongest Doppler spectral component, also corresponds to a group of raindrops with a certain diameter. For convenience, this group of raindrops are regarded as the characteristic raindrops here, and the diameter and velocity of those raindrops are defined as characteristic size D_{c} and characteristic

velocity V_c respectively, i.e.,

$$D_c = \underset{D}{\arg\max}\, \sigma_{hh}(D)N(D). \qquad (7)$$

The polarization channel to obtain the Doppler spectrum is "hh" in this article, and the correspondence among D_c, V_c, and Doppler velocity in still air is shown in Fig. 1. It is worth mentioning that the characteristic velocity is equal to the characteristic raindrops' terminal falling velocity [see Fig. 1(b)] in still air, and this is useful for method's verification, as discussed in Section IV.

For raindrops in a certain radar range bin, the characteristic velocity can be obtained with the Doppler velocity and radar elevation angle. Then, if the characteristic size can be determined, the motion equation of the characteristic raindrops can be established as follows [28]:

$$\frac{d\boldsymbol{v}}{dt} = \boldsymbol{g} + \frac{g}{V_T^2}|\delta\boldsymbol{v}|\delta\boldsymbol{v} \qquad (8)$$

where $\boldsymbol{v}$ and V_T are the velocity and the theoretical terminal falling velocity of the characteristic raindrops, respectively, g is the downward gravitational acceleration, and $\delta\boldsymbol{v}$ is the difference velocity between the background wind and the characteristic raindrops. From (8), the background wind velocity could be decoupled from the characteristic raindrops' velocity when the characteristic size is determined, as shown in Fig. 2. Thus, in this article, the main purpose is to retrieve the characteristic size, i.e., the size of raindrops corresponding to the Doppler velocity.

C. Major Impact Factors of the Characteristic Size

As we can see in (7), the Doppler spectral density and D_c in a certain radar range bin are determined by both $\sigma_{hh}(D)$ and $N(D)$. To retrieve D_c more accurately, they are studied here first.

1) Scattering Property of Raindrops: In general, the RCS of a nonspherical raindrop is determined by the radar wavelength (λ), elevation angle (ϕ), and the orientation of this raindrop. The T-matrix method [29], which is a good RCS simulation toolbox for ellipsoid target, can be used to simulate the RCS of a raindrop in terms of different parameters, for example, radar wavelength, elevation angle, and raindrop's orientation.

$S/C/X$-band radars are widely used for remote sensing in precipitation [30], so we take three representative wavelengths as examples (111 mm for S-band, 53.5 mm for C-band, and 33.3 mm for X-band) to study the impact of wavelength on the RCS of a raindrop. Because the horizontal incidence wave ($\phi = 0°$) cannot detect the terminal falling velocity of raindrops and the vertical incidence case ($\phi = 90°$) is not sensitive to polarimetric information of raindrops, the elevation angles in this study are set in range between $10°$ and $60°$, at a step of $10°$. A raindrop's orientation can generally be determined by two angles α and β (see Fig. 3), where α is the angle between the incidence direction and the symmetry axis of this raindrop, and β, called the canting angle, is the angle between the vertical direction on the plane of polarization and the drop's symmetry axis on the same plane. Generally, α is assumed to obey the uniform distribution in $[0°, 360°]$, and β can be approximated
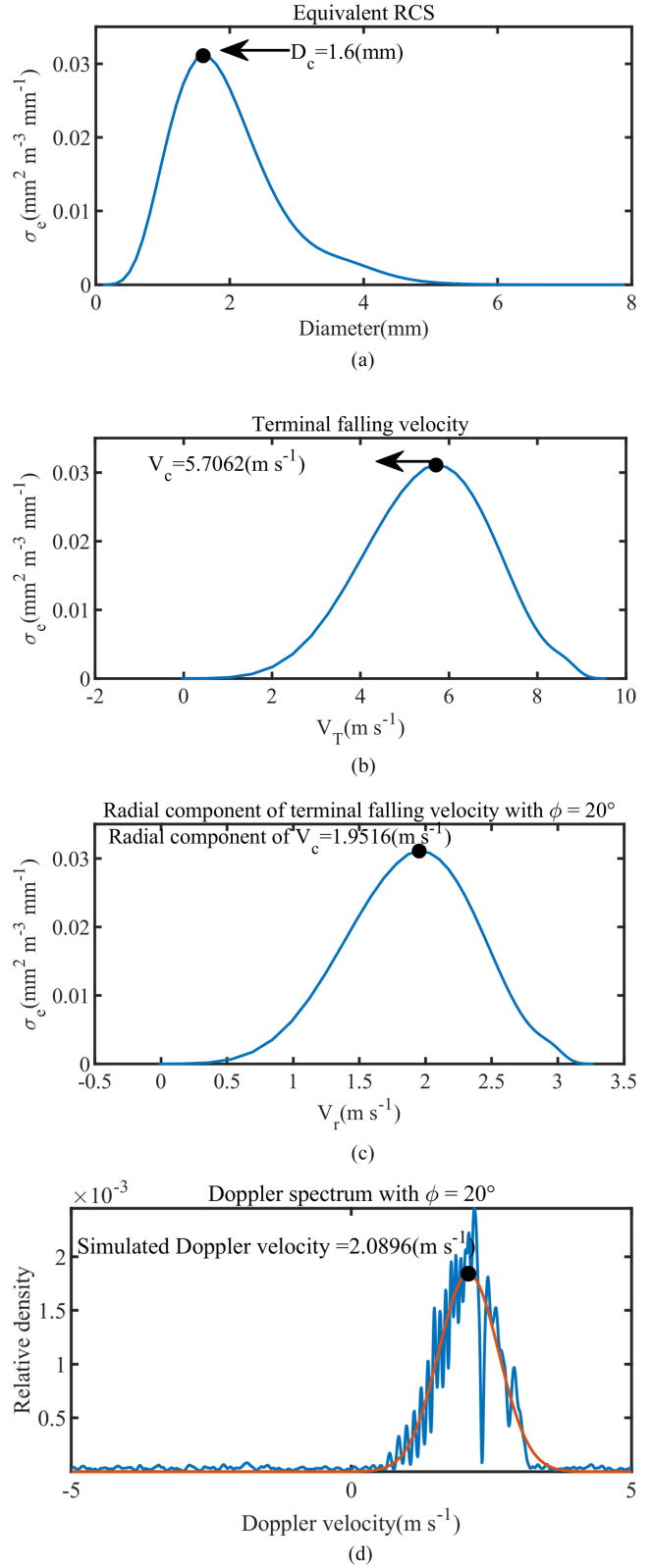

Fig. 1. Correspondence among D_c, V_c, and Doppler velocity of precipitation in a certain radar range bin in still air. This figure is simulated in X-band, with $\phi = 20°$, based on normalized gamma DSD ($N_w = 3000(\mathrm{m}^{-3}\cdot\mathrm{mm}^{-1})$, $D_0 = 1(\mathrm{mm})$, $\mu = 0$). (a) σ_e versus diameter. The numerical relationship between the two is shown in (7), and D_c corresponds to the maximum of the curve. (b) σ_e versus V_T, which is derived from curve in (a) with (1); here, the velocity of a raindrop is just the raindrop's terminal falling velocity due to the hypothesis of still air. (c) σ_e versus V_r, where V_r is the projection of terminal falling velocity on radar beam with $\phi = 20°$. (d) Simulated Doppler spectrum, which is consistent with curve in (c) when noise's impact is ignorable.

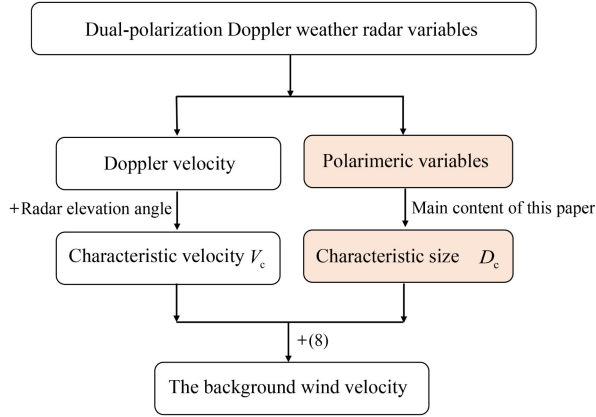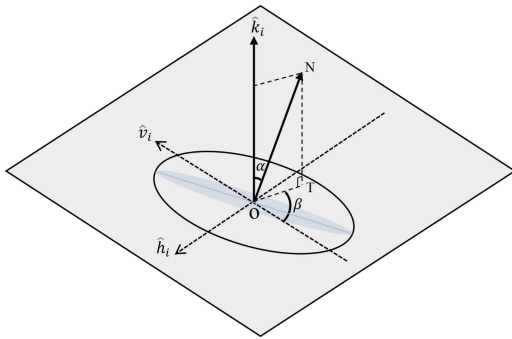Fig. 2. Block scheme for retrieval of the background wind velocity.

Fig. 3. Raindrop's orientation. $\widehat{h_i}/\widehat{v_i}$ is the orientation of horizontal/vertical polarization and $\widehat{k_i}$ is the orientation of the incidence wave. $\overline{ON}$ is the symmetry axis of this raindrop, and $\overline{OT}$ is the projection of the symmetry axis on the plane of polarization. α and β are always used to express the orientation of the raindrop.

with a Gaussian distribution with zero mean and small standard deviation ($6°$ in low wind conditions and $12°$ in moderate wind conditions typically, and rarely smaller than $1°$ or larger than $21°$) [31], [32]. Given that the orientation of raindrops cannot be determined in advance, we only compared the scattering properties for different radar wavelengths and elevation angles in this part.

As shown in Fig. 4(a), the RCS curves for different wavelengths are different from each other. Similarly, the impact of elevation angles is also visible in Fig. 4(b), especially for bigger raindrops whose shape deformations are severer. Besides, bigger raindrops always have bigger RCS, so the equivalent RCS σ_e should present a more special distribution if a DSD includes more big raindrops.

2) DSD of Raindrops and Its Impact on D_c: As shown in (4), the normalized gamma DSD is determined by parameters N_w, D_0, and μ. In this analysis, the parameter N_w is fixed as $N_w = 3000$ since it does not influence the characteristic size D_c, and we try to find out the dependence of D_c on D_0 and μ. Here, D_0 varies in [1.75, 3] and μ varies in [9, 20] with five linearly distributed samples. Part of the simulation results for the concerned S-band radar at $\phi = 10°$, $\overline{\beta} = 0°$, and $\sigma_\beta = 6°$ is shown in Fig. 5. It can be observed that the value of D_c increases with the increase of D_0 and the decrease of μ. Thus, a potential
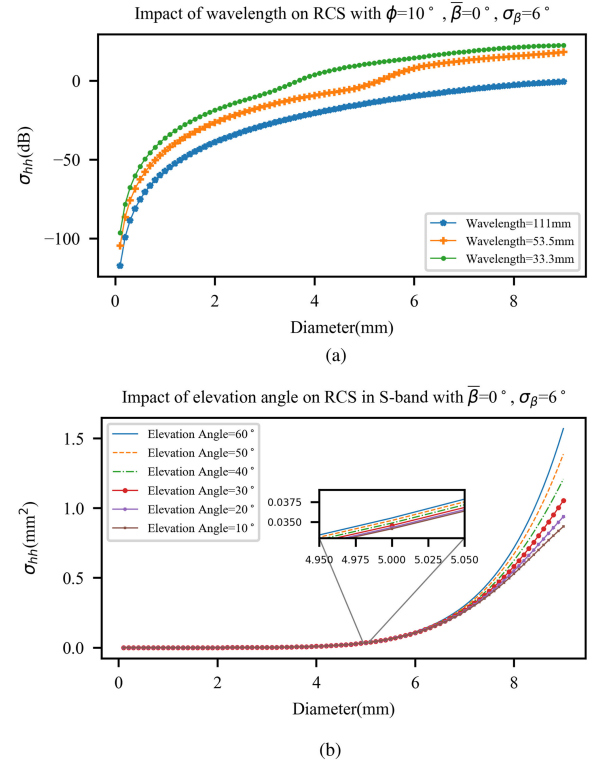

Fig. 4. Major impact factors for the RCS of a single raindrop. (a) Impact of radar wavelengths on the RCS. The elevation angle is $10°$, and the canting angle is set to be a Gaussian distribution with zero mean and standard deviation of $6°$. (b) Impact of elevation angles on the RCS. The wavelength is 111 mm and the canting angle is set to be a Gaussian distribution with zero mean and standard deviation of $6°$.

way to obtain D_c with existing methods is to first retrieve D_0 and μ and then calculate D_c with the retrieved results. During this process, the retrieval of D_0 and μ is the average effect of a lot of observations, and the error accumulation always happens when D_c is obtained from the averaged parameters. To avoid the unnecessary errors, this study aims to propose a new method to retrieve D_c directly from observed polarimetric variables.

III. METHOD TO RETRIEVE THE CHARACTERISTIC SIZE

As discussed in Section II, D_c is mainly influenced by five parameters, say, the radar band, elevation angle, canting angle, the median volume diameter, and the shape parameter of DSD. In radar detection campaigns, only the radar frequency and observing elevation angle are known in advance, so this study aims to retrieve D_c from the radar observing data in terms of different orientation distribution and size distribution of raindrops. Here, the radar in use is assumed to be a dual-polarization radar due to its good ability in characterizing the size and shape of raindrops over large spatial and temporal scales.

A. Relationship Between Polarimetric Variables and Characteristic Size of Raindrops

The polarimetric variables provided by a dual-polarization Doppler weather radar include the radar reflectivity Z_h and Z_v, differential reflectivity Z_{dr}, specific differential phase K_{DP},
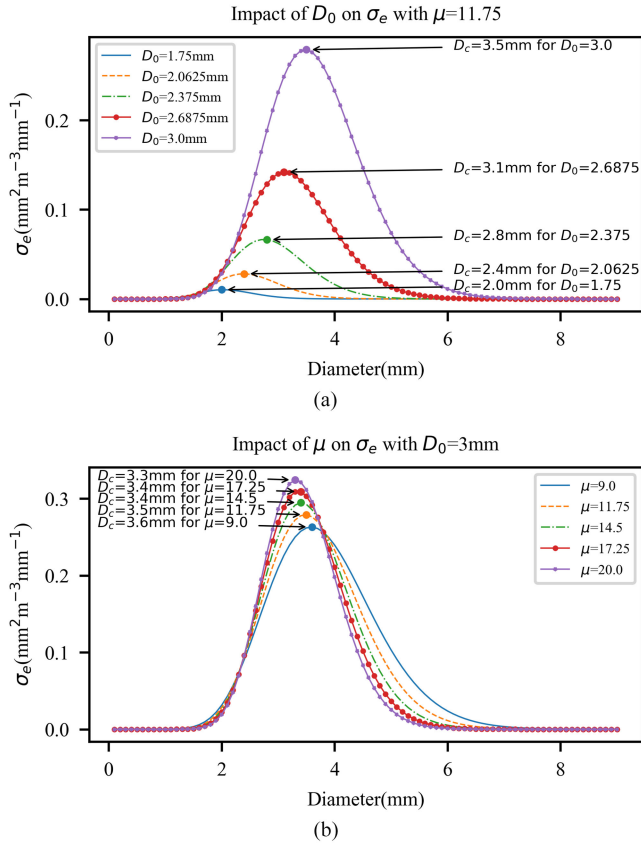
Fig. 5. Impact of normalized gamma DSD parameters on equivalent RCS and raindrops' characteristic size. (a) Impact of D_0. The radar band is S-band, the elevation angle is $10°$, the canting angle is set to be a Gaussian distribution with zero mean and standard deviation of $6°$, and μ is 11. The characteristic size increases with the increase of D_0. (b) Impact of μ. D_0 is 3 mm, and the characteristic size decreases with the increase of μ when the other parameters are the same as in Fig. 4(a).

differential phase shift Φ_{DP}, copolar correlation coefficient ρ_{hv}, and linear depolarization ratio L_{dr}, and $Z_H/Z_{DR}/L_{DR}$ mean the value of $Z_h/Z_{dr}/L_{dr}$ in logarithmic scale [33]. Among them, Z_{dr} and K_{DP} are strongly related to the shape/size of raindrops, but the big influence of canting angle on these two variables may degenerate their ability for representing the shape/size. However, the circular depolarization ratio C_{dr}, which mainly depends on the raindrops' shape, is insensitive to the orientations of raindrops. Even though C_{dr} has such a good property, it is not easy to be obtained directly from a linear polarization radar. Fortunately, the depolarization ratio D_r shown in (9) can serve as a proxy for it, and the impact of propagation effect on D_r is almost negligible from low-frequency radars [34]–[39]. So, in this study, D_r is taken as a key variable to retrieve D_c, and D_R denotes the value of D_r in logarithmic scale

$$D_r = \frac{1 + Z_{dr}^{-1} - 2\rho_{hv}Z_{dr}^{-1/2}}{1 + Z_{dr}^{-1} + 2\rho_{hv}Z_{dr}^{-1/2}}. \quad (9)$$

Simulations based on the T-matrix were carried out to show the relationships between the above polarimetric variables (Z_H, Z_{DR}, K_{DP}, ρ_{hv}, L_{DR}, and D_R) and D_c in terms of different radar and rain parameters shown in Table I [15], where the normalized

TABLE I
PARAMETER SET OF RADAR AND RAINDROPS

Parameter type	Values
Radar wavelength λ	111mm(S-band) 53.5mm(C-band) 33.3mm(X-band)
Elevation angle ϕ	$10°,20°,30°,40°,50°,60°$
Mean canting angle $\overline{\beta}$	$0°,1°,2°$
Standard deviation of $\beta(\sigma_\beta)$	$1°,3°,6°,9°,12°,15°,18°,21°$
Normalized intercept parameter $N_w(\mathrm{m}^{-3} \cdot \mathrm{mm}^{-1})$	9 linearly distributed samples in (1,000, 100,000)
Median diameter $D_0(\mathrm{mm})$	9 linearly distributed samples in (0.5, 3.0)
Shape parameter μ	9 linearly distributed samples in (-2, 20)

gamma DSD was adopted. It is worth noticing that N_w is set to vary in (1000, 100 000) with nine linearly distributed samples in this part, because N_w can also influence the polarimetric variables.

We first take S-band as an example to show the dependence of characteristic size on different polarimetric variables (Z_H, Z_{DR}, K_{DP}, ρ_{hv}, L_{DR}, and D_R), and the simulation results are shown in Fig. 6. In each subfigure, a group of data for a marker are with a certain elevation angle (ϕ), but different settings of canting angles ($\overline{\beta}$, σ_β) and DSD parameters (N_w, D_0, μ). It is obvious that Z_H, K_{DP}, and L_{DR} are not good proxies for D_c because one value of $Z_H/K_{DP}/L_{DR}$ may correspond to two or more very different values of D_c. The copolar correlation coefficient ρ_{hv} almost does not change in the whole range of D_c, so it is not a good proxy for the characteristic size D_c, either.

For the rest two polarimetric variables Z_{DR} and D_R, they are strongly related to the elevation angle, but, fortunately, the elevation angle is generally known in advance. When attention is paid to a certain elevation angle, both Z_{DR} and D_R have a functional relationship with D_c, in detail, an approximately linear relationship for $Z_{DR} \sim D_c$, and an approximately exponential relationship for $D_R \sim D_c$. In terms of that, Z_{DR} seems to be a better choice than D_R because a linear relationship generally leads to a smaller fitting error than an exponential relationship. However, for all the elevation angles, the variation of Z_{DR} depending on canting angles is always much more noticeable than that of D_R. Furthermore, the canting angle's impact on Z_{DR} gets severer as the radar beam gets more slant from the zenith, but that impact on D_R is almost negligible when the elevation angle is around $45°$. From this point of view, both Z_{DR} and D_R have their advantages and disadvantages in determining D_c. If the advantages of the two variables can be integrated, better estimation of D_c might be expected, which has been substantiated by simulation results (see Section III-B) and radar measurements (see Section IV).

B. Retrieval Model and Evaluation

In order to find the best proxy for D_c, retrieval models based on Z_{DR}, D_R, and $Z_{DR} + D_R$ need to be established, respectively; in other words, optimal functions for $D_c = f_1(Z_{DR})$, $D_c = f_2(D_R)$ and $D_c = f_3(Z_{DR}, D_R)$ need to be found in this part. As discussed in Section II and shown in Fig. 6, the
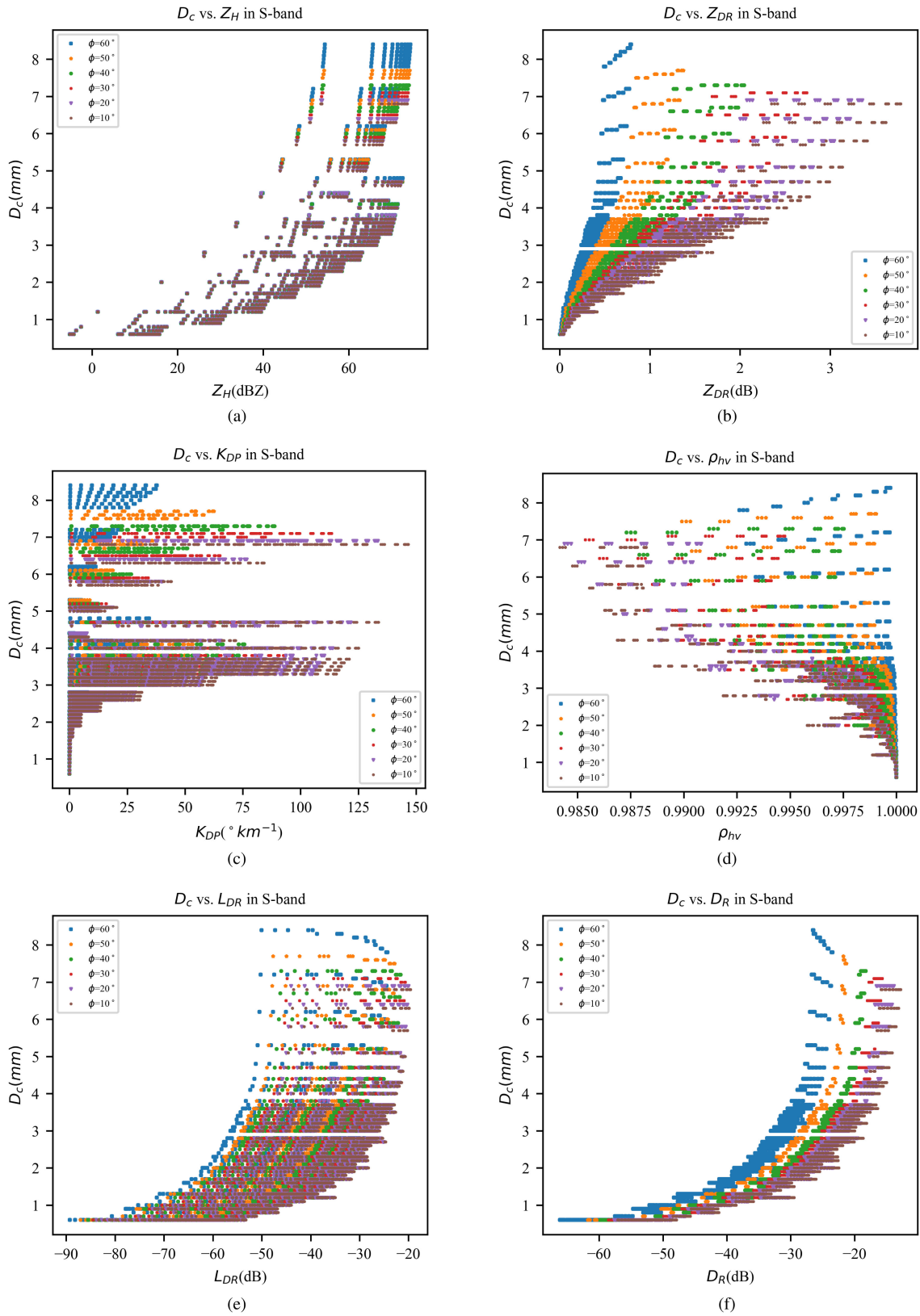
Fig. 6. Relationship between polarimetric variables and D_c in *S*-band. (a) D_c versus Z_H. (b) D_c versus Z_{DR}. (c) D_c versus K_{DP}. (d) D_c versus ρ_{hv}. (e) D_c versus L_{DR}. (f) D_c versus D_R.
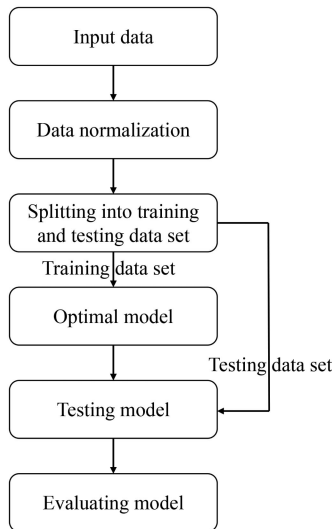
Fig. 7.   Flowchart to build and evaluate the retrieval models.

relationship between $Z_{\mathrm{DR}}/D_{\mathrm{R}}$ and D_{c} changes a lot among different radar bands and elevation angles, so it is better to analyze data for each radar band and elevation angle. It is a fundamental regression issue to establish a retrieval model of D_{c} from $Z_{\mathrm{DR}}/D_{\mathrm{R}}$, and a common tool to deal with that is support vector regression (SVR), which is a derivation of support vector machine with good robustness and efficiency [40]–[42]. The basic idea of SVR is to convert the nonlinear regression in sample space to linear regression in higher dimensional space (feature space) by using kernel functions, and the common kernel functions include linear kernel function and radial basis function (RBF); the former is mainly suitable for linear regression issues and the latter can be used in both linear and nonlinear regression issues [43], [44]. In this study, the relationship between D_{R} and D_{c} is obviously not a linear relationship, so the RBF kernel function is chosen due to its excellent adaptability.

The flowchart to build and evaluate the retrieval models based on simulation data is shown in Fig. 7. First, for each radar band and elevation angle shown in Table I, simulations were carried out to obtain dataset as the input data ($Z_{\mathrm{DR}} \sim D_{\mathrm{c}}$, $D_{\mathrm{R}} \sim D_{\mathrm{c}}$, and $'Z_{\mathrm{DR}} + D'_{\mathrm{R}} \sim D_{\mathrm{c}}$). According to existing studies, DSD varies for different regions [45], [46]. Besides the normalized gamma DSD shown in Section III-A, exponential DSD and gamma DSD for rain cases in a specific region were also taken into account in this part to enrich the experiment results, and the parameters of the two DSDs can be found in [46, Table III]. The next step is data preprocessing, i.e., normalizing the input data and dividing them into training dataset (accounting for 80%) and testing dataset (accounting for 20%). Then, the training dataset was used to establish the optimal model based on SVR, and the testing dataset was used to evaluate that model.

Part of the retrieval models for concerned S-band is shown in Fig. 8. Fig. 8(a) shows the retrieval models based on Z_{DR} for different elevation angles, where different markers mean samples for different elevation angles, and the curves surrounded by each kind of markers are the predicted results with testing dataset and
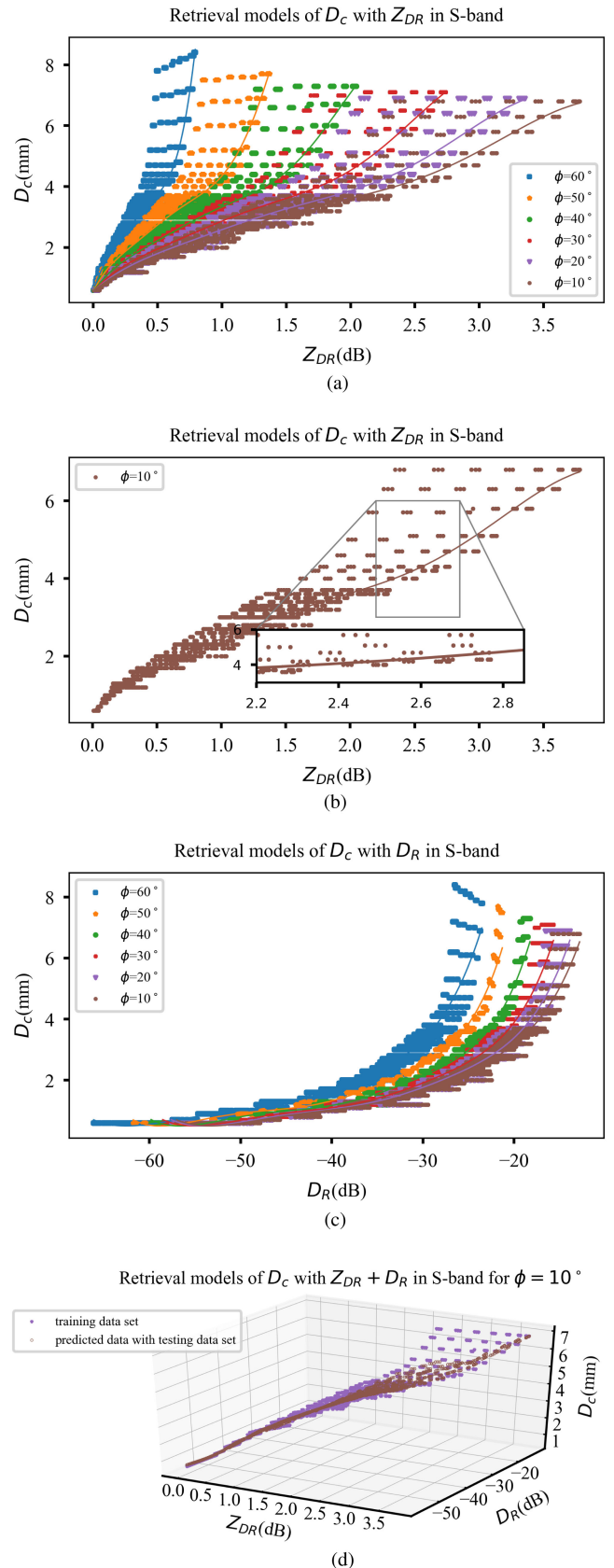

Fig. 8.   Retrieval models in S-band. (a) Retrieval models based on Z_{DR} for different elevation angles. (b) Retrieval models based on Z_{DR} for $\phi = 10°$. (c) Retrieval models based on D_{R} for different elevation angles. (d) Retrieval model based on $Z_{\mathrm{DR}} + D_{\mathrm{R}}$ for $\phi = 10°$.

show the tendency of corresponding retrieval models. It is worth noting that the retrieval model for each elevation angle seems to be off the center of the samples, which is because the samples are denser at the location of the curve, as we can see in the zoom figure in Fig. 8(b). Fig. 8(c) shows the retrieval models based on D_R for different elevation angles. It is observed that the SVR results for D_R are obviously better than the Z_{DR}-related models due to the less diversity of the Z_{DR}-related simulation results. The relationship between fusion result and Z_{DR}/D_R should be a 3-D surface for each elevation angle. For simplicity, here, we only show the retrieval model based on $Z_{DR} + D_R$ for $\phi = 10°$ in S-band [see Fig. 8(d)], where the triangle-down markers ($\triangledown$) mean the training dataset and the point markers ($\cdot$) mean the predicted data with testing dataset.

Even though the predicted data seem to comply well with the training dataset in Fig. 8, the retrieval errors are not intuitive, especially for the fusion models. In this article, the root-mean-square error (RMSE) is used to characterize the performance of the estimation

$$\mathrm{RMSE} = \sqrt{\frac{1}{N} \sum_{i=1}^{N} (y_i - \widehat{y_i})^2} (\mathrm{mm}) \qquad (10)$$

where N is the number of parameters in the testing dataset, y_i is the true value of D_c for the ith sample in the testing dataset, and $\widehat{y_i}$ is an estimation of y_i. Generally speaking, a smaller RMSE means a better retrieval model. Here, process to build and evaluate the retrieval model for each input data was repeated for five times because the procedure to divide the input dataset into training data and testing data is stochastic to some extent, and the averaged evaluation results are shown in Fig. 9.

In Fig. 9, different markers represent different DSD models. In detail, point markers ($\cdot$) and triangle-down markers ($\triangledown$) are related to the exponential DSD and gamma DSD, respectively, and star markers ($\star$) are related to the normalized gamma DSD. On the whole, compared with those from the normalized gamma DSD, models based on dataset derived from the exponential DSD and gamma DSD for a specific region perform better. The reason of this phenomenon is that the precipitation cases described by the normalized gamma DSD are more universal, while the other two DSDs mainly describe cases limited to a specific region. Therefore, the prior information of DSD model type for a specific region is useful to improve the performance of the retrieval models.

For retrieval models based on Z_{DR}, shown by solid lines in Fig. 9, the RMSE increases with the increase of elevation angles, which is mainly caused by the smaller gradients of Z_{DR} for larger elevation angles. For retrieval models based on D_R, shown by dashed lines in Fig. 9, it is clear that the retrieval quality reaches the best when elevation angle is around 45°. This is caused by the fact that the data around 45° are more gathering than those in the rest angles. Therefore, elevation angles around 45° are suggested for retrieval models based on D_R. By comparing the evaluation results of retrieval models based on Z_{DR} and D_R, models based on D_R perform better in most cases. Furthermore, better performance is expected
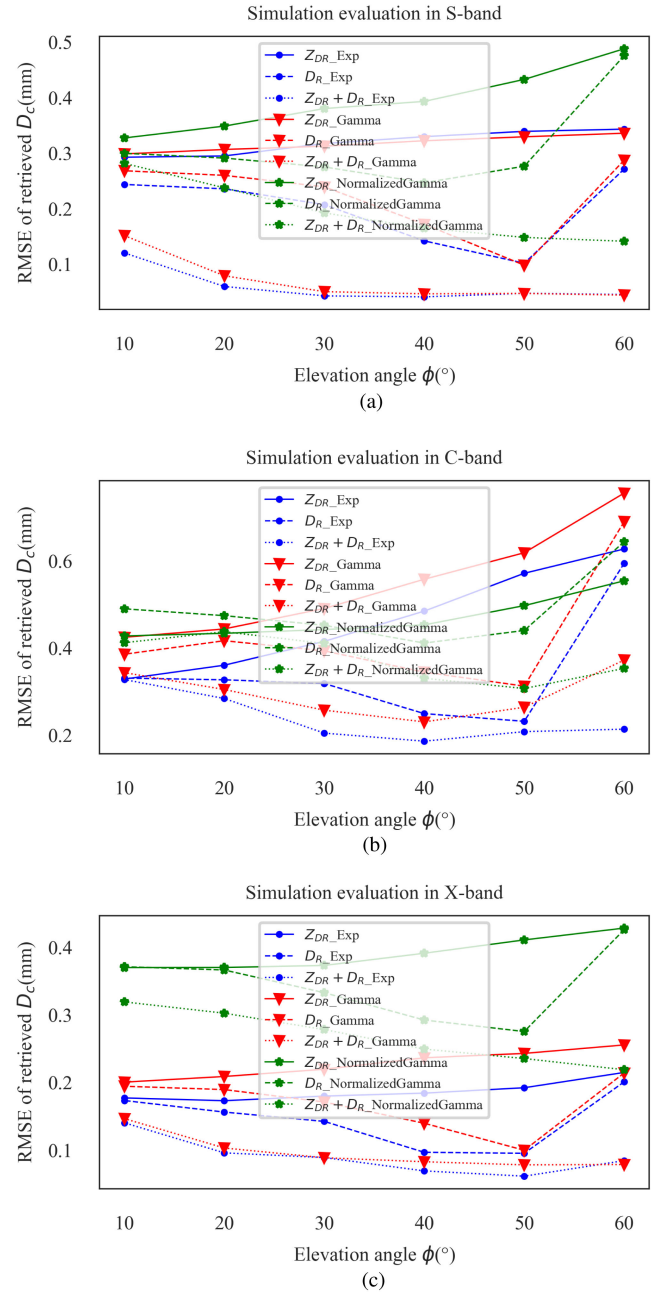

Fig. 9. Evaluation results of retrieval models. (a) RMSE of retrieval models in S-band. (b) RMSE of retrieval models in C-band. (c) RMSE of retrieval models in X-band.

with the fusion models combining both Z_{DR} and D_R, which is actually indicated by the dotted lines in Fig. 9.

IV. METHOD VERIFICATION WITH FIELD OBSERVATION DATA

To better show the performance of the retrieval method proposed in Section III, verification of it with field observation data (radar data and disdrometer data) has been carried out. The radar data around HKIA were collected with an S-band dual linear polarization Doppler weather radar. The elevation angles for observation were 10°, 22°, and 34°, and the product data include Z_{DR}, ρ_{hv}, and Doppler velocity. The disdrometer data
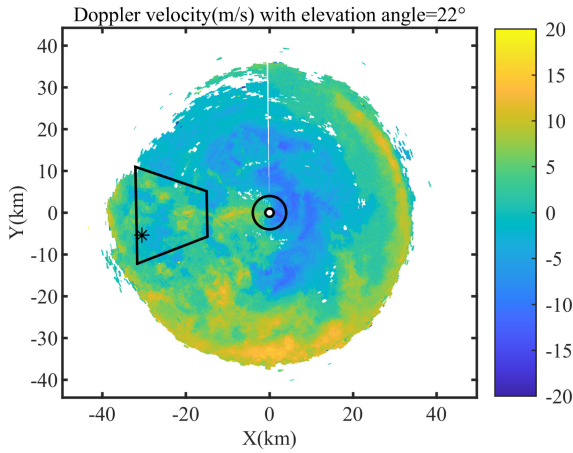
Fig. 10. Doppler velocity of PPI scan around 12:21 UTC on September 30, 2020 with the elevation angle of 22°. The center of this figure is the location of radar and the star marker indicates the location of the disdrometer. The region enclosed by the quadrilateral is where the polarimetric data are selected, while the region between the two rings is where the Doppler velocity data are selected.

were collected with a 2-D video disdrometer, which was located at an azimuth of 260° and 31 km away from the radar, as shown by the star marker ($\star$) in Fig. 10.

A. Verification of the Retrieved Characteristic Size

As said above, the polarimetric variables of radar data can be used to retrieve the raindrops' characteristic size. And the DSD obtained from the disdrometer can also be used to directly calculate D_c with the scattering property of raindrops, which can be treated as the benchmark to evaluate D_c retrieved from the radar data. On September 30, 2020, May 4, 2021, and June 1, 2021, rain cases were detected by the disdrometer and radar, and the dataset are used to verify the proposed method. With the disdrometer data, the DSD can be computed with [47]

$$N(D_i) = \frac{1}{\Delta T \Delta D} \sum_{j=1} \frac{1}{A_j v_j} (\mathrm{m}^{-3} \cdot \mathrm{mm}^{-1}) \qquad (11)$$

where D_i is the diameter of category i, ΔT is the integration time (300 s in this study), ΔD is the width of the size class (0.1 mm in this study), A_j is the disdrometer effective measurement area during the collection of drop j, and v_j is the falling velocity of raindrop j. According to the radar scanning frequency, the time frame was set with an interval of 6 min. Then, the equivalent RCS at each time frame can be computed with (6), which can be fitted to a Gaussian curve to get an estimation of D_c with (7). The equivalent RCS around 12:21 UTC on September 30, 2020 is shown in Fig. 11.

Considering the relative location of radar and disdrometer, the radar data of azimuth in range from 250° to 290° and radial distance from 16 to 34 km were selected here to guarantee the correlation of data from different instruments, as shown by the quadrilateral in Fig. 10. After basic quality control of the data (for example, Z_{DR} is limited in [0.5, 3], which is a value range of Z_{DR} in previous studies [33], [34], [48] and in our simulation), D_R was calculated with Z_{DR} and ρ_{hv} by (9); then, Z_{DR} and D_R of different elevation angles were input to the SVR model
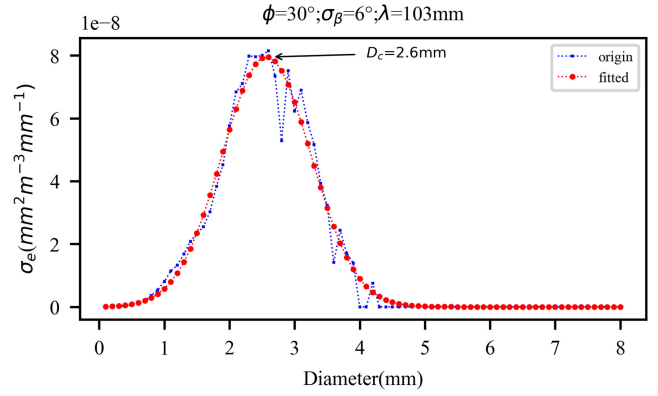

Fig. 11. σ_e and D_c calculated with $\phi = 30°$, $\sigma_\beta = 6°$, and $\lambda = 103$ mm around 12:21 UTC on September 30, 2020. The result is averaged in 5 min. The blue line is the original σ_e calculated with (6) and the red line is the Gaussian curve fit of the data.

TABLE II
RMSE OF RETRIEVED D_c FOR THREE RAIN CASES

No.	ϕ	RMSE($D_c^{Z_{DR}}$)	RMSE($D_c^{D_R}$)	RMSE($D_c^{Z_{DR}+D_R}$)
	10°	0.7901	0.7514	0.6066
1	22°	0.7021	0.6645	0.5505
	34°	0.9714	0.8823	0.5924
	10°	0.9057	0.8962	0.7282
2	22°	0.8228	0.8312	0.7184
	34°	1.2257	1.1203	0.8156
	10°	0.5677	0.5360	0.4454
3	22°	0.8732	0.7941	0.4989
	34°	1.3050	1.1302	0.6567
average		0.9071	0.8451	**0.6236**

trained by simulation data in Section III. During the process of comparison and verification, one kind of characteristic size $D_c^{Disdrometer}$ can be obtained by combining the disdrometer data and the scattering property of raindrops, and other three kinds of characteristic size, i.e., $D_c^{Z_{DR}}$, $D_c^{D_R}$, and $D_c^{Z_{DR}+D_R}$, can be obtained from the retrieval models based on Z_{DR}, D_R, and the fusion models of $Z_{DR} + D_R$, respectively. For a certain elevation angle at each time frame, the RMSE of retrieved D_c is shown in Fig. 12, where the benchmark is $D_c^{Disdrometer}$ obtained from the disdrometer data, the solid/dashed lines mean the RMSE of D_c retrieved with models based on Z_{DR}/D_R, and the dotted lines mean the RMSE of D_c retrieved with the fusion models. To make it clearer, the RMSE of retrieved D_c from radar data is shown in Table II, where the data corresponding to each ϕ in each case is the averaged value for time frames. It is obvious that the fusion models combining the information of Z_{DR} and D_R always perform better for all the three cases; this phenomenon meets well with the conclusion of simulation results in Section III.

B. Verification of the Velocity of the Characteristic Raindrops

The main purpose of this study is to retrieve D_c and analyze the interaction between raindrops and the background wind, which can provide basic model support to retrieve the background wind velocity in the further study. As we can see in (8), if the background wind field is comparatively stable, the
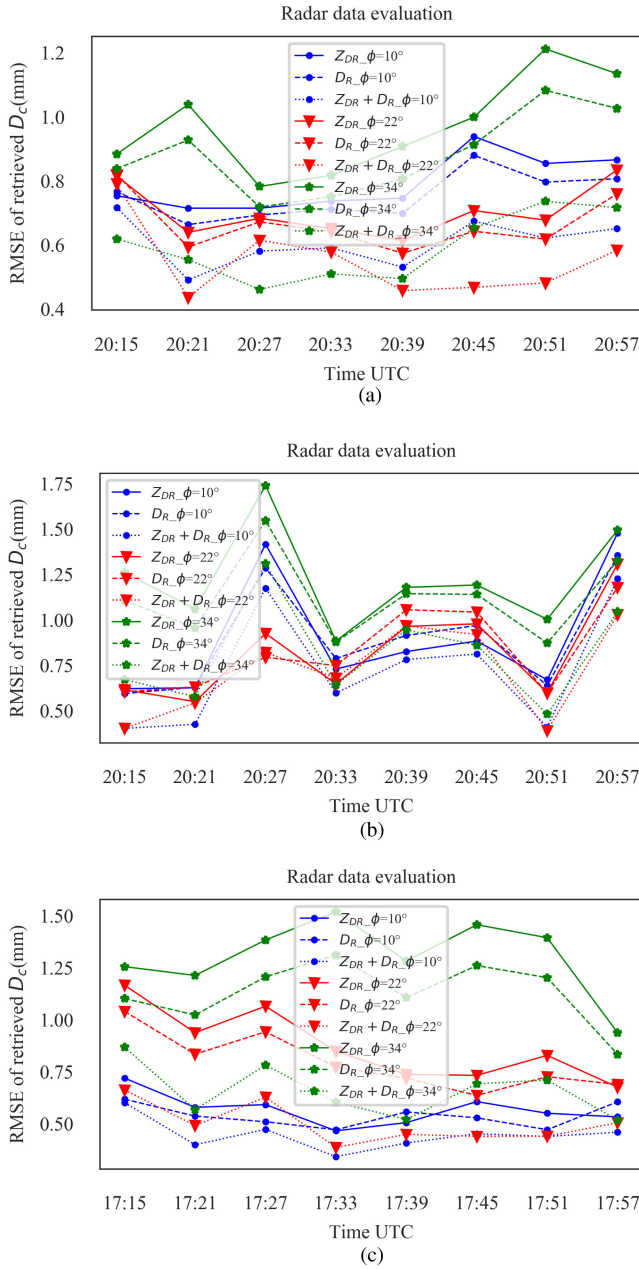
Fig. 12. RMSE of retrieved D_c for different retrieval models, where the radar data come from an S-band dual-polarization radar and the benchmark is D_c calculated with disdrometer data. (a) Model evaluation with data detected on September 30, 2020. (b) Model evaluation with data detected on May 4, 2021. (c) Model evaluation with data detected on June 1, 2021.

horizontal velocity component of the characteristic raindrops should be identical to that of the background wind, while the velocity difference between the characteristic raindrops and the background wind in vertical orientation should be equal to the terminal falling velocity of the characteristic raindrops (V_T), i.e.,

$$\delta v_z = v_z^{D_c} - v_z^b = V_T^{D_c} \qquad (12)$$

where $v_z^{D_c}$ is the vertical velocity component of the characteristic raindrops, v_z^b is that component of the background wind velocity, and $V_T^{D_c}$ is the terminal falling velocity of the characteristic
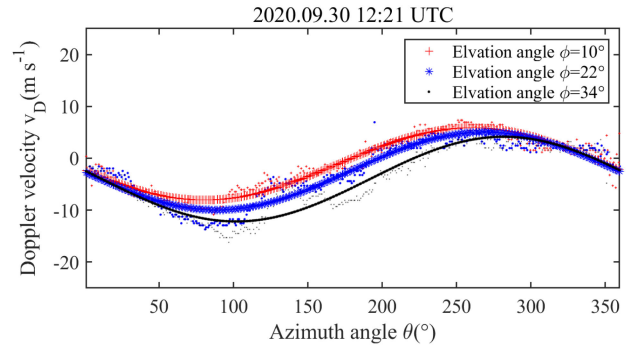

Fig. 13. Relationship between v_D and θ. This figure comes from the radar data around 12:21 UTC on September 30, 2020 with different elevation angles, and the radial distance is 1 km.

raindrops [see (1)]. In other words, $v_z^{D_c}$ should be equal to the sum of v_z^b and $V_T^{D_c}$, and this relationship can be used to evaluate the retrieval models of D_c proposed in Section III. Theoretically, we need to know v_z^b when we evaluate the D_c retrieval models based on (12); however, due to the limited experimental conditions, we did not have any anemometer to detect v_z^b at high altitude (this problem may be solved by using unmanned-aerial-vehicle-based anemometer [49] in our further work). So, we chose the radar data under comparatively stable air condition for velocity verification, where v_z^b is approximately equal to zero.

With the Doppler velocity detected by radar, the vertical velocity component of the raindrops can be obtained with the velocity–azimuth display (VAD) method if the background wind obeys a linear distribution model [50]. For a certain radar range bin at azimuth angle θ and elevation angle ϕ, the Doppler velocity can be written as [11]

$$v_D = u \cos\theta \cos\phi + v \sin\theta \cos\phi + w \sin\phi \qquad (13)$$

where u and v are the horizontal components and w is the vertical component of the characteristic raindrops' velocity. For a certain region, the characteristic raindrops' velocity can be seen as a constant when assuming a uniform wind field. Then, for a specific elevation angle, there should be a trigonometric function relationship between v_D and θ, i.e.,

$$v_D = \sqrt{u^2 + v^2} \cos\phi \sin(\theta + \theta_0) + w \sin\phi \qquad (14)$$

where $\theta_0 = \sin^{-1}(u/\sqrt{u^2 + v^2})$. After data quality control (for example, removing abnormal v_D with 3-Sigma method, i.e., calculating mean value $\overline{x}$ and standard deviation σ_x of samples, and outlier beyond $[\overline{x} - 3\sigma_x, \overline{x} + 3\sigma_x]$ is removed), the observation data can be fitted to a trigonometric function to obtain the three components of the characteristic raindrops' velocity, i.e., u, v, and w, and w is just $v_z^{D_c}$ said above. Fig. 13 presents three groups of data and fit curves, and the good agreement between the observation data and the triangular fit curves confirms the stable air condition in selected region.

Fig. 14 shows the comparison results of velocities retrieved with different methods around 12:21 UTC on September 30, 2020. In the figure, the solid lines mean the terminal falling velocity of $D_c^{Disdrometer}$, the dashed lines mean $v_z^{D_c}$ derived
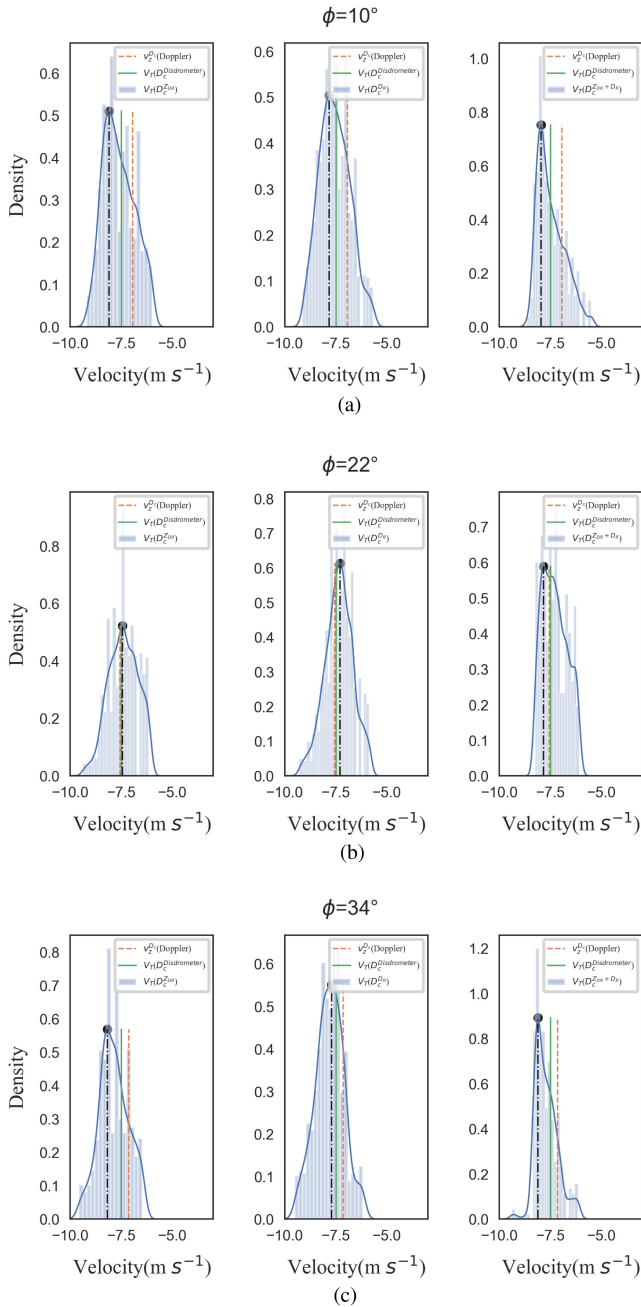
Fig. 14. Comparison results of velocities retrieved with different methods around 12:21 UTC on September 30, 2020. (a) Comparison result for $\phi = 10°$. (b) Comparison result for $\phi = 22°$. (c) Comparison result for $\phi = 34°$.

TABLE III
RMSE OF RETRIEVED VELOCITIES WHEN THE BENCHMARK IS $V_{\mathrm{T}}(D_{\mathrm{c}}^{\mathrm{Disdrometer}})$

ϕ \ RMSE	$V_{\mathrm{T}}(D_{\mathrm{c}}^{Z_{\mathrm{DR}}})$	$V_{\mathrm{T}}(D_{\mathrm{c}}^{D_{\mathrm{R}}})$	$V_{\mathrm{T}}(D_{\mathrm{c}}^{Z_{\mathrm{DR}}+D_{\mathrm{R}}})$
10°	0.77	0.74	0.67
22°	0.72	0.70	0.63
34°	0.81	0.76	0.59

TABLE IV
RMSE OF RETRIEVED VELOCITIES WHEN THE BENCHMARK IS $v_{\mathrm{z}}^{D_{\mathrm{c}}}$ (DOPPLER)

ϕ \ RMSE	$V_{\mathrm{T}}(D_{\mathrm{c}}^{Z_{\mathrm{DR}}})$	$V_{\mathrm{T}}(D_{\mathrm{c}}^{D_{\mathrm{R}}})$	$V_{\mathrm{T}}(D_{\mathrm{c}}^{Z_{\mathrm{DR}}+D_{\mathrm{R}}})$
10°	1.02	0.95	0.85
22°	0.73	0.71	0.66
34°	1.02	0.96	0.78

First, good agreement between $V_{\mathrm{T}}(D_{\mathrm{c}}^{\mathrm{Disdrometer}})$ and $v_{\mathrm{z}}^{D_{\mathrm{c}}}$ (Doppler) indicates that the velocity of the characteristic raindrops determined by the equivalent RCS is a potential proxy of the Doppler velocity of that group of raindrops. Besides, the difference between $V_{\mathrm{T}}(D_{\mathrm{c}}^{\mathrm{Disdrometer}})$ and $v_{\mathrm{z}}^{D_{\mathrm{c}}}$ (Doppler) might be caused by two factors: 1) errors from the velocity retrieval method VAD and 2) the vertical component $v_{\mathrm{z}}^{\mathrm{b}}$ of the background wind is approximately set as zero. If $v_{\mathrm{z}}^{\mathrm{b}}$ can be measured by an instrument in the experiment, better agreement between $v_{\mathrm{z}}^{D_{\mathrm{c}}}$ (Doppler) and $v_{\mathrm{z}}^{\mathrm{b}} + V_{\mathrm{T}}(D_{\mathrm{c}}^{\mathrm{Disdrometer}})$ is expected.

Second, based on the comparison of the RMSE, we can see that the terminal falling velocity corresponding to the characteristic size ($D_{\mathrm{c}}^{Z_{\mathrm{DR}}}$, $D_{\mathrm{c}}^{D_{\mathrm{R}}}$, and $D_{\mathrm{c}}^{Z_{\mathrm{DR}}+D_{\mathrm{R}}}$) obtained from polarimetric variables is almost equal to the vertical component $v_{\mathrm{z}}^{D_{\mathrm{c}}}$ (Doppler) of raindrops' velocity, and $V_{\mathrm{T}}(D_{\mathrm{c}}^{Z_{\mathrm{DR}}+D_{\mathrm{R}}})$ has the smallest difference to $v_{\mathrm{z}}^{D_{\mathrm{c}}}$ (Doppler) compared with $V_{\mathrm{T}}(D_{\mathrm{c}}^{Z_{\mathrm{DR}}})$ and $V_{\mathrm{T}}(D_{\mathrm{c}}^{D_{\mathrm{R}}})$. Therefore, the characteristic size retrieval method based on polarimetric variables works well to represent the motion behavior of raindrops, and the fusion model based on $Z_{\mathrm{DR}} + D_{\mathrm{R}}$ has the best performance.

On the whole, the results of radar data test indicate that the retrieval of background wind velocity with the information of D_{c} is feasible, and further velocity verification should be made if we can deploy an accurate velocity measurement instrument in the high sky to get the background wind component $v_{\mathrm{z}}^{\mathrm{b}}$.

V. CONCLUSION

In this study, the raindrops' characteristic size D_{c} is defined, which corresponds to the strongest Doppler spectral component and can be used to retrieve the velocity of background wind in the further study. Then, the relationship between D_{c} and polarimetric variables is analyzed for different radar bands and elevation angles to find a good retrieval model for D_{c}. Finally, experiments based on simulation results and field radar data show that:

1) both differential reflectivity (Z_{DR}) and the depolarization ratio (D_{R}) can serve as proxies for D_{c}, while D_{R} performs better than Z_{DR} in most cases, especially when the elevation angle is around 45°;

from the Doppler velocity with VAD method, and the three histograms in each subplot represent the terminal falling velocity distribution of $D_{\mathrm{c}}^{Z_{\mathrm{DR}}}$, $D_{\mathrm{c}}^{D_{\mathrm{R}}}$, and $D_{\mathrm{c}}^{Z_{\mathrm{DR}}+D_{\mathrm{R}}}$, respectively. The solid curves are the fit curves of those histograms, and the maximum of each curve is marked by the dash-dotted line. The RMSEs of retrieved terminal falling velocities for different characteristic sizes ($D_{\mathrm{c}}^{Z_{\mathrm{DR}}}$, $D_{\mathrm{c}}^{D_{\mathrm{R}}}$, and $D_{\mathrm{c}}^{Z_{\mathrm{DR}}+D_{\mathrm{R}}}$) with different benchmarks [$V_{\mathrm{T}}(D_{\mathrm{c}}^{\mathrm{Disdrometer}})$ and $v_{\mathrm{z}}^{D_{\mathrm{c}}}$ (Doppler)] are shown in Tables III and IV. Two phenomena found in Fig. 14 and Tables III and IV are as follows.

2) the fusion model based on Z_{DR} and D_R performs even better than D_R because it combines the advantages of Z_{DR} and D_R;

3) the retrieval of background wind velocity with the information of D_c is feasible.

In this article, the characteristic size of raindrops has been well defined and verified. This can build a good connection between the characteristic raindrops' velocity and the background wind velocity when the inertia of raindrops is considered. Because the integrating process is based on fitting and training the existing data, the performance of the fusion model is related to data quality and universality. Thus, efforts should be made to improve the applicability of the present method to other DSD models and observation data and further to retrieve the background wind velocity based on the motion equation of the characteristic raindrops in more complex cases. This is on our near future work schedule.

REFERENCES

[1] Y. Liu, S. Li, P. W. Chan, and D. Chen, "Empirical correction ratio and scale factor to project the extreme wind speed profile for offshore wind energy exploitation," *IEEE Trans. Sustain. Energy*, vol. 9, no. 3, pp. 1030–1040, Jul. 2018.

[2] H. Gao, J. Li, P. W. Chan, K. K. Hon, and X. Wang, "Parameter-retrieval of dry-air wake vortices with a scanning Doppler Lidar," *Opt. Exp.*, vol. 26, pp. 16377–16392, Jun. 2018.

[3] R. Frehlich and N. Kelley, "Measurements of wind and turbulence profiles with scanning Doppler Lidar for wind energy applications," *IEEE J. Sel. Topics Appl. Earth Observ. Remote Sens.*, vol. 1, no. 1, pp. 42–47, Mar. 2008.

[4] C. S. Ruf, S. Gleason, and D. S. McKague, "Assessment of CYGNSS wind speed retrieval uncertainty," *IEEE J. Sel. Topics Appl. Earth Observ. Remote Sens.*, vol. 12, no. 1, pp. 87–97, Jan. 2019.

[5] X. Chu *et al.*, "Multimodal deep learning for heterogeneous GNSS-R data fusion and ocean wind speed retrieval," *IEEE J. Sel. Topics Appl. Earth Observ. Remote Sens.*, vol. 13, pp. 5971–5981, 2020.

[6] J. E. Stopa, A. A. Mouche, B. Chapron, and F. Collard, "Sea state impacts on wind speed retrievals from C-band radars," *IEEE J. Sel. Topics Appl. Earth Observ. Remote Sens.*, vol. 10, no. 5, pp. 2147–2155, May 2017.

[7] J. Kainulainen *et al.*, "Airborne wind vector scatterometer for sea surface measurements," *IEEE J. Sel. Topics Appl. Earth Observ. Remote Sens.*, vol. 12, no. 7, pp. 2470–2476, Jul. 2019.

[8] W. Huang, E. Gill, X. Wu, and L. Li, "Measurement of sea surface wind direction using bistatic high-frequency radar," *IEEE Trans. Geosci. Remote Sens.*, vol. 50, no. 10, pp. 4117–4122, Oct. 2012.

[9] X. Liu, W. Huang, and E. W. Gill, "Wind direction estimation from rain-contaminated marine radar data using the ensemble empirical mode decomposition method," *IEEE Trans. Geosci. Remote Sens.*, vol. 55, no. 3, pp. 1833–1841, Mar. 2017.

[10] H. Chen and V. Chandrasekar, "Real-time wind velocity retrieval in the precipitation system using high-resolution operational multi-radar network," in *Remote Sensing of Aerosols, Clouds, and Precipitation*. Amsterdam, The Netherlands: Elsevier, 2018, pp. 315–339.

[11] Y. Wang, M. Wei, Z. Wang, S. Zhang, and L. Liu, "Novel scanning strategy for future spaceborne Doppler weather radar with application to tropical cyclones," *IEEE J. Sel. Topics Appl. Earth Observ. Remote Sens.*, vol. 10, no. 6, pp. 2685–2693, Jun. 2017.

[12] L. Pfitzenmaier, Y. Dufournet, C. M. H. Unal, and H. W. J. Russchenberg, "Retrieving fall streaks within cloud systems using Doppler radar," *J. Atmos. Ocean. Technol.*, vol. 34, no. 4, pp. 905–920, 2017.

[13] S. Lovejoy and D. Schertzer, "Turbulence, raindrops and the l(1/2) number density law," *New J. Phys.*, vol. 10, no. 7, 2008, Art. no. 0 75017.

[14] T. A. Seliga and V. N. Bringi, "Potential use of radar differential reflectivity measurements at orthogonal polarizations for measuring precipitation," *J. Appl. Meteorol. Climatol.*, vol. 15, no. 1, pp. 69–76, 1976.

[15] C. W. Ulbrich, "Natural variations in the analytical form of the raindrop size distribution," *J. Appl. Meteorol. Climatol.*, vol. 22, no. 10, pp. 1764–1775, 1983.

[16] P. T. Willis, "Functional fits to some observed drop size distributions and parameterization of rain," *J. Atmos. Sci.*, vol. 41, no. 9, pp. 1648–1661, 1984.

[17] G. Zhang, J. Vivekanandan, and E. Brandes, "A method for estimating rain rate and drop size distribution from polarimetric radar measurements," *IEEE Trans. Geosci. Remote Sens.*, vol. 39, no. 4, pp. 830–841, Apr. 2001.

[18] E. Gorgucci, V. Chandrasekar, V. N. Bringi, and G. Scarchilli, "Estimation of raindrop size distribution parameters from polarimetric radar measurements," *J. Atmos. Sci.*, vol. 59, no. 15, pp. 2373–2384, 2002.

[19] E. Gorgucci, V. Chandrasekar, G. Scarchilli, and S. Bolen, "Variation of mean raindrop shape derived from polarimetric radar measurements," *Atmos. Res.*, vol. 59/60, pp. 283–293, Oct. 2001.

[20] H. R. Pruppacher and R. L. Pitter, "A semi-empirical determination of the shape of cloud and rain drops," *J. Atmos. Sci.*, vol. 28, no. 1, pp. 86–94, 1971.

[21] M. Thurai, G. J. Huang, V. Bringi, W. Randeu, and M. Schoenhuber, "Drop shapes, model comparisons, and calculations of polarimetric radar parameters in rain," *J. Atmosp. Ocean. Technol.*, vol. 24, no. 6, pp. 1019–1032, 2007.

[22] D. Atlas, R.C. Srivastava, and R. S. Sekhon, "Doppler radar characteristics of precipitation at vertical incidence," *Rev. Geophys.*, vol. 11, no. 1, pp. 1–35, 1973.

[23] A. Waldvogel, "The n0 jump of raindrop spectra," *J. Atmos. Sci.*, vol. 31, pp. 1067–1078, Apr. 1974.

[24] C. Caracciolo, F. Porcù, and F. Prodi, "Precipitation classification at mid-latitudes in terms of drop size distribution parameters," *Adv. Geosci.*, vol. 16, no. 6, pp. 11–17, 2008.

[25] L. S. Kumar, Y. H. Lee, and J. T. Ong, "Two-parameter gamma drop size distribution models for Singapore," *IEEE Trans. Geosci. Remote Sens.*, vol. 49, no. 9, pp. 3371–3380, Sep. 2011.

[26] T. Islam, M. A. Rico-Ramirez, M. Thurai, and D. Han, "Characteristics of raindrop spectra as normalized gamma distribution from a Joss-Waldvogel disdrometer," *Atmos. Res.*, vol. 108, pp. 57–73, 2012.

[27] D. N. Moisseev and V. Chandrasekar, "Nonparametric estimation of raindrop size distributions from dual-polarization radar spectral observations," *J. Atmos. Ocean. Technol.*, vol. 24, no. 6, pp. 1008–1018, 2007.

[28] Z. Liu, N. Jeannin, F. Vincent, and X. Wang, "Modeling the radar signature of raindrops in aircraft wake vortices," *J. Atmos. Ocean. Technol.*, vol. 30, no. 3, pp. 470–484, 2013.

[29] J. Leinonen, "High-level interface to t-matrix scattering calculations: Architecture, capabilities and limitations," *Opt. Exp.*, vol. 22, pp. 1655–1660, Jan. 2014.

[30] A. T. Zadeh, M. Mälzer, J. Simon, S. Beck, J. Moll, and V. Krozer, "Range-Doppler analysis for rain detection at Ka-band: Numerical and experimental results from laboratory and field measurements," *IEEE J. Sel. Topics Appl. Earth Observ. Remote Sens.*, vol. 13, pp. 1027–1033, 2020.

[31] G. J. Huang, V. N. Bringi, and M. Thurai, "Orientation angle distributions of drops after an 80-m fall using a 2D video disdrometer," *J. Atmos. Ocean. Technol.*, vol. 25, no. 9, pp. 1717–1723, 2008.

[32] V. N. Bringi, M. Thurai, and D. A. Brunkow, "Measurements and inferences of raindrop canting angles," *Electron. Lett.*, vol. 44, no. 24, pp. 1425–1426, 2008.

[33] V. Bringi and V. Chandrasekar, *Polarimetric Doppler Weather Radar: Principles and Operations*. Cambridge, U.K.: Cambridge Univ. Press, Oct. 2001.

[34] A. Ryzhkov *et al.*, "Estimation of depolarization ratio using weather radars with simultaneous transmission/reception," *J. Appl. Meteorol. Climatol.*, vol. 56, no. 7, pp. 1797–1816, 2017.

[35] A. Ryzhkov, P. Zhang, Q. Cao, S. Matrosov, V. Melnikov, and M. Knight, "Measurements of circular depolarization ratio with the radar with simultaneous transmission/reception," *Meteorol. Climatol.*, vol. 56, pp. 1797–1816, 2017.

[36] S. Y. Matrosov, C. G. Schmitt, M. Maahn, and G. de Boer, "Atmospheric ice particle shape estimates from polarimetric radar measurements and in situ observations," *J. Atmosp. Ocean. Technol.*, vol. 34, no. 12, pp. 2569–2587, 2017.

[37] S. Y. Matrosov, "Ice hydrometeor shape estimations using polarimetric operational and research radar measurements," *Atmosphere*, vol. 11, no. 1, 2020, Art. no. 97.

[38] S. Y. Matrosov, A. V. Ryzhkov, M. Maahn, and G. D. Boer, "Hydrometeor shape variability in snowfall as retrieved from polarimetric radar measurements," *J. Appl. Meteorol. Climatol.*, vol. 59, no. 9, pp. 1–36, 2020.

[39] J. Yin, H. Chen, Y. Li, and X. Wang, "Clutter mitigation based on spectral depolarization ratio for dual-polarization weather radars," *IEEE J. Sel. Topics Appl. Earth Observ. Remote Sens.*, vol. 14, pp. 6131–6145, 2021.

[40] C. Cortes and V. Vapnik, "Support vector networks," *Mach. Learn.*, vol. 20, pp. 273–297, 1995.

[41] A. D. Mehr, V. Nourani, V. Khosrowshahi, and M. A. Ghorbani, "A hybrid support vector regression-firefly model for monthly rainfall forecasting," *Int. J. Environ. Sci. Technol.*, vol. 16, pp. 1–12, May 2018.

[42] E. Olyaie, H. Z. Abyaneh, and A. D. Mehr, "A comparative analysis among computational intelligence techniques for dissolved oxygen prediction in Delaware river," *Geosci. Front.*, vol. 8, no. 3, pp. 517–527, 2017.

[43] W. Chen, Z.-J. Fu, and C.-S. Chen, *Recent Advances in Radial Basis Function Collocation Methods*. Berlin, Germany: Springer-Verlag, 2013.

[44] M. N. Jebur, B. Pradhan, and M. S. Tehrany, "Manifestation of LiDAR-derived parameters in the spatial prediction of landslides using novel ensemble evidential belief functions and support vector machine models in GIS," *IEEE J. Sel. Topics Appl. Earth Observ. Remote Sens.*, vol. 8, no. 2, pp. 674–690, Feb. 2015.

[45] S. Das, A. Maitra, and A. Shukla, "Rain attenuation modeling in the 10-100 GHz frequency using drop size distributions for different climatic zones in tropical India," *Prog. Electromagn. Res. B*, vol. 25, pp. 211–224, Jan. 2010.

[46] D. Sumbiri and T. J. O. Afullo, "Optimized rain drop size distribution model for microwave propagation for equatorial Africa," *SAIEE Afr. Res. J.*, vol. 111, no. 1, pp. 22–35, 2020.

[47] T. J. Schuur, A. V. Ryzhkov, D. S. Zrnić, and M. Schoenhuber, "Drop size distributions measured by a 2D video disdrometer: Comparison with dual-polarization radar data," *J. Appl. Meteorol.*, vol. 40, no. 6, pp. 1019–1034, 2001.

[48] C. A. Knight, L. J. Miller, and R. A. Rilling, "Aspects of precipitation development in trade wind cumulus revealed by differential reflectivity at S band," *J. Atmos. Sci.*, vol. 65, no. 8, pp. 2563–2580, 2008.

[49] J. Yin, P. Hoogeboom, C. Unal, H. Russchenberg, F. van der Zwan, and E. Oudejans, "UAV-aided weather radar calibration," *IEEE Trans. Geosci. Remote Sens.*, vol. 57, no. 12, pp. 10362–10375, Dec. 2019.

[50] G. Teschke and V. Lehmann, "Mean wind vector estimation using the velocity-azimuth display (VAD) method: An explicit algebraic solution," *Atmos. Meas. Techn.*, vol. 10, no. 9, pp. 3265–3271, 2017.

Yunli Peng was born in 1997. She received the B.E. degree in electronic information engineering from the Chengdu University of Information Technology, Chengdu, China, in 2019. She is currently working toward the M.E. degree in electronic and communication engineering with the College of Electronic Science and Engineering, National University of Defense Technology, Changsha, China.

Her research interests include the radar characteristics and the detection of distribution soft target.

Jianbing Li (Senior Member, IEEE) was born in 1979. He received the B.E. and M.E. degrees in aerospace science from the College of Aerospace Science and Engineering, National University of Defense Technology (NUDT), Changsha, China, in 2002 and 2004, respectively, and the Ph.D. degree in information and communication engineering for his work on the analysis of wake vortices' scattering characteristics from the College of Electronic Science and Engineering, NUDT, in 2010.

He is currently a Full Professor with the College of Electronic Science and Engineering, NUDT. His research interests include radar characteristics and detection of distributed soft target.

Dr. Li received outstanding Scientific and Technical Worker Award of Chinese Institute of Electronics. His Ph.D. dissertation was awarded as a candidate of the National Outstanding Ph.D. dissertations in China in 2013. He was also elected as an Outstanding Young Scholar in Hunan Province, China.

Jiapeng Yin received the B.Sc. degree in information engineering from the National University of Defense Technology (NUDT), Changsha, China, in 2012, and the Ph.D. degree in atmospheric remote sensing from the Delft University of Technology, Delft, The Netherlands, in 2019.

He is currently an Assistant Professor with the College of Electronic Science and Technology, NUDT. His research interests include radar polarimetry, polarimetric weather radar, radar signal processing, and radar calibration.

Pak Wai Chan received the B.Sc. degree in physics and maths and the M.Phil. degree in physics from the University of Hong Kong, in 1992 and 1994, respectively.

He is an Assistant Director of the Hong Kong Observatory, Hong Kong, responsible for weather forecasting and warning services for the public. Prior to this, he has been working with the Hong Kong International Airport for more than 20 years, with research and operational efforts in airport meteorological instrumentation, low-level windshear and turbulence alerting, and high-resolution numerical weather prediction. He is a visiting Professor of a number of universities in mainland China and an adjunct Associate Professor with the University of Hong Kong, Hong Kong. He has authored or coauthored more than 260 papers in SCI journals, with a significant portion of the papers focusing on the applications at the airport.

Prof. Chan is a Fellow of the Royal Meteorological Society and a Chartered Meteorologist. He is a Vice Chair of the Expert Team of Upper Air Measurement at World Meteorological Organization and a Chair of a working group of the International Civil Aviation Organization in Asian region.

Wai Kong received the B.Sc. degree in major in physics and minor in mathematics and the M.Phil. degree in physics from the Chinese University of Hong Kong, in 2004 and 2006, respectively.

He has been with the Hong Kong Observatory, Hong Kong, since 2009. He is currently responsible for the provision of weather monitoring, forecasting, and warning services for the public and government departments, and coordinating the development and implementation of forecasting services on high-impact extreme weather. He has worked for the weather radar operation, calibration and maintenance of the Hong Kong Observatory for ten years, overseeing the development of new radar applications and radar-related research, experiments, and training.

Mr. Kong is the member of the Joint Expert Team on Operational Weather Radar, World Meteorological Organization.

Xuesong Wang was born in 1972. He received the B.Sc. and Ph.D. degrees in information and communication engineering from the College of Electronic Science and Engineering, National University of Defense Technology (NUDT), Changsha, China, in 1994 and 1999, respectively.

He is currently a Professor with NUDT, where he is also the Dean of the College of Science. His research interests concentrate on radar information processing and target recognition.

Dr. Wang is a Fellow of the Chinese Institute of Electronics. His Ph.D. dissertation was awarded as one of the 100 excellent Ph.D. dissertations in China in 2001 (two years after his graduation).